One-Stop-Shop for Modeling Optical Frequency Comb Generation

Ergun Simsek*, Alioune Niang[†], Pradyoth Shandilya[‡], Logan Courtright[§], Raonaqul Islam[¶], Gary Carter[∥], and Curtis R. Menyuk**

Department of Computer Science and Electrical Engineering, Center for Navigation, Timing & Frequency Research, University of Maryland Baltimore County, Baltimore, MD 21250, USA *simsek@umbc.edu, †aniang1@umbc.edu, ‡shandilya@umbc.edu, §lcourt1@umbc.edu, ¶raonaqi1@umbc.edu, ||carter@umbc.edu, **menyuk@umbc.edu

Abstract—This paper presents a comprehensive study of optical frequency comb generation in a silicon nitride microresonator coupled to a silicon nitride waveguide. We provide a complete numerical framework combining mode solvers, coupled-mode theory, and the Lugiato-Lefever equation to accurately model the system. Both numerical simulations and experimental measurements demonstrate the generation of a frequency comb with a 99.6 GHz free spectral range, characterized by a resonant linewidth (full width at half maximum) of 120 MHz, corresponding to a high quality factor of 1.6 million. Discrepancies between the calculated and experimental spectra are attributed to experimental limitations, such as photodetector noise and fabrication imperfections.

Index Terms—Dielectric waveguides, dielectric rings, coupled mode theory, Lugiato-Lefever equation, optical frequency comb generation.

I. INTRODUCTION

Optical frequency combs, generated via nonlinear processes in microresonators, have emerged as a transformative technology for producing coherent, equally spaced spectral lines from a single laser source. As illustrated in Fig. 1, this process begins when a continuous-wave laser excites a dielectric waveguide coupled to a microresonator (e.g., a ring resonator), generating an optical field into the cavity. Inside the microresonator, strong light confinement and nonlinear effects—primarily four-wave mixing—broaden the pump spectrum, creating a comb-like output [1]-[8]. Frequency combs have become indispensable across diverse fields due to their exceptional stability and precision. For instance, they serve as the backbone for optical atomic clocks [4], enable ultrafast spectroscopy [5], and enhance high-capacity telecommunications through wavelength-division multiplexing [6]. Moreover, their applications extend to microwave photonics and fundamental physics, where they provide unmatched frequency references for testing physical constants and quantum phenomena [7].

To analyze the efficiency, stability, and spectral characteristics of frequency comb generation, it is essential to determine the electromagnetic modes within both the dielectric waveguide and the microresonator. Coupled-mode theory (CMT) [2], [8]–[11] and the Lugiato-Lefever Equation (LLE) [12]–[16] are widely used to model the linear and nonlinear dynamics of frequency comb formation in microresonators, but

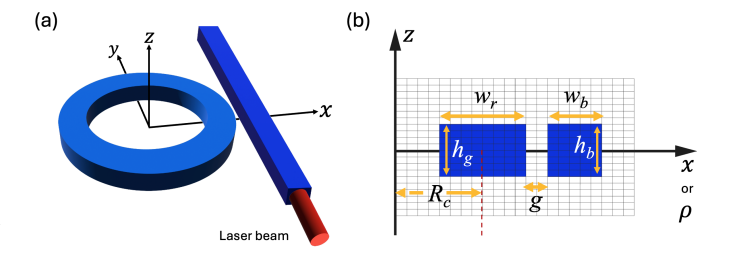


Fig. 1. A dielectric bus waveguide next to a dielectric ring: (a) three- and (b) two-dimensional views. The ring is centered at the origin. R_c , w_r , and h_r are the ring's central radius, width, and height. g is the gap between the ring and waveguide. w_b and h_b are the bus waveguide's width and height. The bus waveguide is excited with a laser at the wavelength of λ . The computation domain is meshed with a rectangular grid on the xz (or ρz) plane. The mesh density is set to $\lambda/30$.

these require accurate mode characterization. Key parameters such as resonance frequencies, effective mode volumes $(V_{\rm eff})$, nonlinear coefficient (γ) , first and second-order dispersion coefficients $(D_1$ and $D_2)$ can be determined through numerical mode solvers. Then, these parameters can be incorporated into CMT [2], [9]–[11] to obtain the transmission spectrum around the resonance wavelength and quality factor (Q). In the final steps, these features can be incorporated into LLE [12]–[16] to analyze the nonlinear nature of the frequency comb generation.

In this work, we first provide compact formulations to calculate the modes of electromagnetic waves propagating in dielectric waveguides and rings. Since the final equations are non-linear, we use the shooting method [17], [18] to find the resonant modes. Second, we use CMT [2], [9]–[11] for analyzing energy transfer between the waveguide and resonator, capturing the resonance conditions and modal interactions critical for optical frequency comb design. Third, we briefly describe how we solve the LLE [12]–[16] to predict the generation of a frequency comb over a wide range of frequencies. After explaining our experimental characterization setup, we provide comparisons of our numerical and experimental results, and we conclude.

II. FORMULATION: MODE SOLVERS

A. Dielectric Waveguide Mode Solver

Assume an infinitely long dielectric waveguide with a width of w_b and thickness of h_b is placed parallel to the y-axis

as illustrated in Fig. 1 (a). It is excited with a laser light with a wavelength of λ . The electric field component of the electromagnetic wave propagating inside the dielectric waveguide is given by the following expression using the phasor notation

$$\mathbf{E}(x,y,z) = [\hat{x}E_x(x,z) + \hat{y}E_y(x,z) + \hat{z}E_z(x,z)]e^{-j\beta_b y},$$
(1)

where β_b is the propagation constant of the mode concentrated in the dielectric waveguide. Since the fields outside the waveguide decay exponentially [19], we do not assume two different propagation constants, e.g., one for the fields inside and another one for the fields outside the waveguide.

To determine the field profiles and the propagation constant, we substitute Eq. (1) into the vector wave equation for the electric field given by

$$\nabla^2 \mathbf{E} + \nabla \left(\frac{1}{\varepsilon} \nabla \varepsilon \cdot \mathbf{E} \right) + k_0^2 \varepsilon_r \mathbf{E} = 0, \tag{2}$$

where $k_0 = \omega \sqrt{\mu_0 \varepsilon_0}$ is the free-space wavenumber, and $\varepsilon_r = \varepsilon/\varepsilon_0$ is the relative permittivity, which is a function of position. Then, we expand all the terms in Cartesian coordinates, obtain three equations, and cast these equations into the following matrix equation

$$\begin{bmatrix} M_1 & M_2 & M_3 \\ M_4 & M_5 & M_6 \\ M_7 & M_8 & M_9 \end{bmatrix} \begin{bmatrix} E_x \\ E_y \\ E_z \end{bmatrix} = \beta_b^2 \begin{bmatrix} E_x \\ E_y \\ E_z \end{bmatrix},$$
(3)

where

$$M_1 = M_5 + \frac{\partial}{\partial x} \frac{1}{\varepsilon} \frac{\partial \varepsilon}{\partial x},\tag{4}$$

$$M_2 = M_8 = 0,$$
 (5)

$$M_3 = \frac{\partial}{\partial x} \frac{1}{\varepsilon} \frac{\partial \varepsilon}{\partial z},\tag{6}$$

$$M_4 = -j\beta_b \frac{1}{\varepsilon} \frac{\partial \varepsilon}{\partial x},\tag{7}$$

$$M_5 = \frac{\partial^2}{\partial x^2} + \frac{\partial^2}{\partial z^2} + k_0^2 \varepsilon_r, \tag{8}$$

$$M_6 = -j\beta_b \frac{1}{\varepsilon} \frac{\partial \varepsilon}{\partial z},\tag{9}$$

$$M_7 = \frac{\partial}{\partial z} \frac{1}{\varepsilon} \frac{\partial \varepsilon}{\partial x},\tag{10}$$

$$M_9 = M_5 + \frac{\partial}{\partial z} \frac{1}{\varepsilon} \frac{\partial \varepsilon}{\partial z}.$$
 (11)

The unknown quantity β_b appears in Eqs. (7) and (9). This quantity must be determined in parallel with the field components, as we will discuss shortly.

B. Dielectric Ring Mode Solver

We follow a similar procedure in the cylindrical coordinate system to determine the field profiles and propagation constant for an electromagnetic wave confined in a dielectric ring.

Assume a dielectric ring with a central radius of R_c is placed at the origin as illustrated in Fig. 1. When an electromagnetic wave propagates inside this ring without any loss, in other words, when the resonance condition is satisfied, then the phasor term should have an $e^{-jm\phi}$ dependence, where $m=\beta R_c$

is an integer representing the azimuthal mode order and β is the propagation constant. Then, the electric (E) and magnetic (H) fields can be represented as sums of three orthogonal vectors as follows due to the cylindrical symmetry

$$\mathbf{E}(\rho,\phi,z) = \left\{\hat{\rho}E_{\rho}(\rho,z) + \hat{\phi}E_{\phi}(\rho,z) + \hat{z}E_{z}(\rho,z)\right\}e^{-jm\phi},\tag{12}$$

$$\mathbf{H}(\rho,\phi,z) = \left\{ \hat{\rho}H_{\rho}(\rho,z) + \hat{\phi}H_{\phi}(\rho,z) + \hat{z}H_{z}(\rho,z) \right\} e^{-jm\phi},\tag{13}$$

where ρ is the radial distance from the origin to the point projected onto the xy plane, ϕ is the azimuthal angle, and z is the height or vertical distance from the xy plane.

We derive the wave equations in cylindrical coordinates from Maxwell's equations. Then we express H_{ϕ} in terms of E_z and E_{ρ} and express E_{ϕ} in terms of H_z and H_{ρ} and obtain a set of equations. After moving all the terms with m^2 to the right sides, replacing those m^2 s with $\beta^2 R_c^2$'s, and multiplying both sides of all equations with ρ^2/R_c^2 , we cast the final versions of equations into the following matrix equation

$$\begin{bmatrix} M_{1} & M_{2} & M_{3} & M_{4} \\ M_{5} & M_{6} & M_{7} & M_{8} \\ M_{9} & M_{10} & M_{11} & M_{12} \\ M_{13} & M_{14} & M_{15} & M_{16} \end{bmatrix} \begin{bmatrix} E_{\rho} \\ E_{z} \\ H_{\rho} \\ H_{z} \end{bmatrix} = \beta^{2} \begin{bmatrix} E_{\rho} \\ E_{z} \\ H_{\rho} \\ H_{z} \end{bmatrix}, \quad (14)$$

where

$$M_1 = \mathcal{L} - \frac{1}{R_c^2} + \frac{\rho^2}{R_c^2} \frac{\partial}{\partial \rho} \frac{1}{\varepsilon} \frac{\partial \varepsilon}{\partial \rho}$$
 (15)

$$M_2 = \frac{\rho^2}{R_c^2} \frac{\partial}{\partial \rho} \frac{1}{\varepsilon} \frac{\partial \varepsilon}{\partial z}$$
 (16)

$$M_3 = \frac{2m}{\omega \epsilon R_c^2} \frac{\partial H_\rho}{\partial z} \tag{17}$$

$$M_4 = -\frac{2m}{\omega \epsilon R_c^2} \frac{\partial H_z}{\partial \rho} \tag{18}$$

$$M_5 = \frac{\rho^2}{R_c^2} \frac{\partial}{\partial z} \frac{1}{\varepsilon} \frac{\partial \varepsilon}{\partial \rho} \tag{19}$$

$$M_6 = \mathcal{L} + \frac{\rho^2}{R_c^2} \frac{\partial}{\partial z} \frac{1}{\varepsilon} \frac{\partial \varepsilon}{\partial z}$$
 (20)

$$M_7 = 0 \tag{21}$$

$$M_8 = 0 \tag{22}$$

$$M_9 = -\frac{2m}{\omega \mu_0 R_c^2} \frac{\partial}{\partial z} \tag{23}$$

$$M_{10} = \frac{2m}{\omega \mu_0 R_c^2} \frac{\partial}{\partial \rho} \tag{24}$$

$$M_{11} = \mathcal{L} - \frac{\rho^2}{R_z^2} \frac{1}{\epsilon} \frac{\partial \epsilon}{\partial z} \frac{\partial}{\partial z} - \frac{1}{R_z^2}$$
 (25)

$$M_{12} = \frac{\rho^2}{R_c^2} \frac{1}{\epsilon} \frac{\partial \epsilon}{\partial z} \frac{\partial}{\partial z}$$
 (26)

$$M_{13} = 0$$
 (27)

$$M_{14} = 0$$
 (28)

$$M_{15} = \frac{\rho^2}{R_c^2} \frac{1}{\epsilon} \frac{\partial \epsilon}{\partial \rho} \frac{\partial}{\partial z}$$
 (29)

$$M_{16} = \mathcal{L} - \frac{\rho^2}{R_o^2} \frac{1}{\epsilon} \frac{\partial \epsilon}{\partial \rho} \frac{\partial}{\partial \rho}$$
 (30)

The unknown quantity m appears in Eqs. (17), (18), (23) and (24).

C. Shooting Method

Since we have the unknown propagation constant β_b and m in the first and second Hamiltonians, respectively, we first use approximate β_b [17] and m [18] values to solve the Eqs. (3) and (14), and we obtain approximate eigenvalues (propagation constants). Then, we use these new propagation constants to form the new Hamiltonian matrices and solve the matrix equations again. We repeat this process till the differences between the previous and current eigenvalues are negligibly small.

D. Numerical Solution with Finite Differences

We discretize the computational domain along a rectangular grid by selecting N_x (or N_ρ) uniformly distributed samples along the x (or ρ) direction for the dielectric waveguide (ring) and N_z uniformly distributed samples along the z-direction. We approximate the first-order derivatives $\partial f/\partial \zeta$ and second-order derivatives $\partial^2 f/\partial \zeta^2$ at a point ζ using the following fourth-order stencil formulas

$$\frac{\partial f}{\partial \zeta} \approx \frac{-f(\zeta+2h)+8f(\zeta+h)-8f(\zeta-h)+f(\zeta-2h)}{12h},$$
 (31)

$$\frac{\partial^2 f}{\partial \zeta^2} \approx \frac{-f(\zeta+2h)+16f(\zeta+h)-30f(\zeta)+16f(\zeta-h)-f(\zeta-2h)}{12h^2}, (32)$$

where h is the unit mesh length along the ζ direction.

We impose Neumann boundary conditions [20] by setting the normal derivatives of the field to zero at the outer boundaries of the computational domain.

III. CMT, FOUR-PORT MODEL, AND LLE

Assume that now we have both a dielectric waveguide and a dielectric ring resonator. They are separated by a gap g. The electric and magnetic field distributions of the fundamental modes in the waveguide and resonator are denoted as \mathbf{E}_w , \mathbf{H}_w and \mathbf{E}_r , \mathbf{H}_r , respectively, which are determined with our mode solvers. The coupling strength between the two modes is governed by the overlap integral:

$$\Gamma = \frac{\omega \varepsilon_0}{4} \int_V (\mathbf{E}_w^* \cdot \mathbf{E}_r + Z_0^2 \mathbf{H}_w^* \cdot \mathbf{H}_r) dV, \tag{33}$$

where ω is the angular frequency of the optical mode and Z_0 is the impedance of free space.

The mode overlap factor is given by the normalized integral of the fields in the coupling region:

$$\kappa^{2} = \frac{\left| \int_{V_{\text{gap}}} (\mathbf{E}_{w}^{*} \cdot \mathbf{E}_{r} + Z_{0}^{2} \mathbf{H}_{w}^{*} \cdot \mathbf{H}_{r}) dV \right|}{\sqrt{\int_{V_{w}} |\mathbf{E}_{w}|^{2} dV \int_{V_{w}} |\mathbf{E}_{r}|^{2} dV}}.$$
 (34)

Note that κ^2 is dimensionless, and it determines the efficiency of energy transfer between the waveguide and the ring resonator

The four-port model, as depicted in Fig. 2, treats the bus waveguide as if it is made from input and output waveguides connected through a resonant ring cavity. The optical fields in



Fig. 2. A four-port system consisting of a bus dielectric waveguide and a ring resonator. The parameter a_1 represents the incident wave amplitude at the input port of the waveguide, while b_2 is the amplitude of the wave coupled from the waveguide to the ring. This wave travels through the ring, and its amplitude becomes a_4 after experiencing propagation effects such as phase shift and attenuation.

the system are described by the coupling matrix:

$$\begin{bmatrix} \tau & -j\kappa \\ -j\kappa & \tau \end{bmatrix} \begin{bmatrix} a_1 \\ a_4 \end{bmatrix} = \begin{bmatrix} b_2 \\ b_3 \end{bmatrix}$$
 (35)

where τ is the transmission coefficients, respectively, and satisfy the relation $|\tau|^2 + |\kappa|^2 = 1$. The field circulating inside the resonator undergoes attenuation and phase accumulation, leading to the relation: $a_4 = b_3 e^{-\alpha L} e^{-j\beta L}$, where α is the loss coefficient.

We define $\xi = e^{-\alpha L}$ and $\theta = \beta L$ to analyze the system's transmission properties. The power transmission ratio from port a_1 to port b_2 is then given by

$$\left| \frac{b_2}{a_1} \right|^2 = \frac{\tau^2 + \xi^2 - 2\xi\tau\cos\theta}{1 + \tau^2\xi^2 - 2\xi\tau\cos\theta},\tag{36}$$

which characterizes the frequency-dependent response of the system, essential for understanding comb generation.

The coupling quality factor, Q_c , determines how efficiently energy is coupled into the resonator and is given by:

$$Q_c = \frac{k_0 n_g L}{\kappa^2},\tag{37}$$

where $k_0 = \omega/c_0$ and $L = 2\pi R_c$ is the round-trip length of the resonator.

The group index, which describes the dispersion properties of the ring resonator, is given by:

$$n_g = n_{\text{eff}}^{\text{ring}}|_{f_0} + f_0 \left(\frac{n_{\text{eff}}^{\text{ring}}|_{f_0 + \Delta f} - n_{\text{eff}}^{\text{ring}}|_{f - \Delta f}}{2\Delta f} \right), \quad (38)$$

where $n_{\rm eff}^{\rm ring}=\beta/k_0=\beta\lambda_0/2\pi$ is the effective refractive index of the ring at a given frequency. Once n_g is determined, then we can estimate the free spectral range (FSR) with the following approximate formula

$$FSR_{approx} \approx \frac{c_0}{2\pi n_a R_c}.$$
 (39)

Note that we can obtain the second-order dispersion coefficient (D_2) , which is needed for the LLE solver, with the following expression

$$D_2 = -\frac{c}{\omega^3} \left[2\omega \frac{dn_{\text{eff}}^{\text{ring}}}{d\omega} + \omega^2 \frac{d^2 n_{\text{eff}}^{\text{ring}}}{d\omega^2} \right].$$

As previously mentioned, we can also solve the LLE, given by the following formula, to study frequency comb generation

$$\frac{\partial E}{\partial t} = -\left(\frac{1}{2\tau_p} + i\delta_0\right)E + i\frac{n_2}{n_0}|E|^2E + iD_2\frac{\partial^2 E}{\partial \theta^2} + F, \tag{40}$$

where $\tau_p=1/\Delta_{\rm FWHM}$ is the photon lifetime, $\Delta_{\rm FWHM}$ is the resonance linewidth, $\delta_0=\omega_p-\omega_0$ is the pump-resonance detuning, ω_p is the pump frequency, ω_0 is the closest resonance frequency of the microresonator, n_0 is the linear refractive index of the resonator material, n_2 is the nonlinear refractive index (Kerr nonlinearity), θ represents the azimuthal angle around the microresonator, and F is the external continuous wave pump field [12]–[16].

We employ a split-step Fourier method to efficiently and accurately solve the LLE for time evolution [14]. This approach leverages the computational advantages of solving linear and nonlinear components in their respective domains. Specifically, the linear part is solved in the Fourier domain, while the nonlinear part is solved in the azimuthal domain. To mitigate first-order inaccuracies arising from the non-commutative nature of these operations, we implement a symmetric second-order splitting scheme. This involves solving the linear part for half a step, followed by a full step for the nonlinear part, and concluding with another half-step for the linear part. This symmetric splitting minimizes computational cost while maintaining a second-order accuracy [14].

IV. EXPERIMENTAL SETUP

Figure 3 depicts the experimental setup designed to investigate frequency comb formation dynamics, spectral broadening, and coherence properties. This system utilizes a primary pump laser to initiate soliton frequency comb generation through nonlinear effects such as Kerr nonlinearity and four-wave mixing. An auxiliary laser is employed to stabilize the resonator power and expand the soliton access window. Optical isolators are placed after each laser to suppress back reflections. The pump light is amplified by an erbium-doped fiber amplifier (EDFA) to enhance the signal strength before being directed into the microresonator via a circulator. A second circulator routes the output signal towards multiple diagnostic instruments and enables the injection of the auxiliary laser into the resonator in the opposite direction of the primary pump. Two photodetectors convert the optical signals into electrical signals, allowing for time-domain pulse train analysis on an oscilloscope. An optical spectrum analyzer is used to capture and analyze the spectral characteristics of the generated comb.

V. NUMERICAL AND EXPERIMENTAL RESULTS

We investigate frequency comb generation both experimentally and numerically, utilizing a high-Q microresonator based on a silicon nitride (Si₃N₄) ring waveguide. The central radius of the ring resonator is $R_c=225\,\mu m$, with a ring width of $w_r=1.55\,\mu m$ and a height of $h_r=0.8\,\mu m$. The bus waveguide, which couples light into the resonator, has identical cross-sectional dimensions (1.55 $\mu m \times 0.8\,\mu m$). The gap between the waveguide and ring is $g=0.5\,\mu m$.

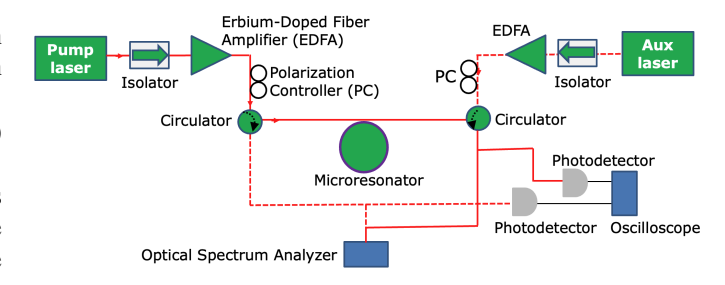


Fig. 3. Schematic of the experimental setup for frequency comb generation and analysis. The red solid lines indicate the primary laser path for soliton frequency comb generation, while the red dashed lines represent the auxiliary laser used to compensate for the resonator's thermal shift. The output is analyzed using photodetectors, an oscilloscope, and an optical spectrum analyzer.

The waveguide and ring resonator are fabricated from $\mathrm{Si}_3\mathrm{N}_4$. The surrounding cladding material is SiO_2 . For numerical calculations, the propagation loss is assumed to be $\alpha=0.06$ dB/cm.

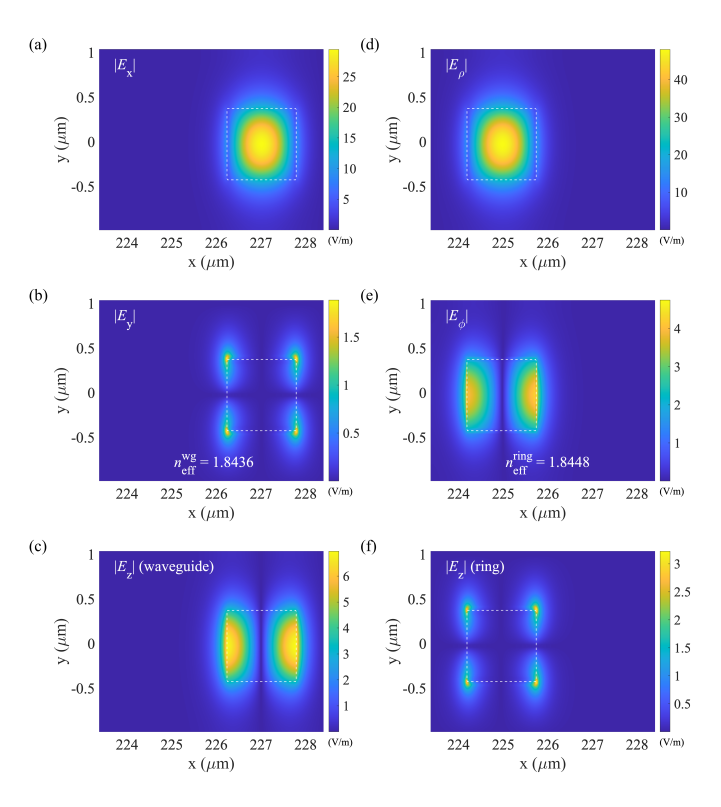


Fig. 4. Electric field intensity of the orthogonal components of the first resonant modes inside the dielectric waveguide (left) and ring (right). White dashed lines indicate the positions of the dielectric waveguide and ring.

For the numerical solution, we use a 200 by 80 grid with a 25 nm mesh length along the horizontal and vertical axes. Figures 4 (a)–(c) show the x, y, and z components of the electric field inside the dielectric waveguide for the first resonant mode determined with the numerical solution of Eq. (3) assuming an excitation wavelength of $\lambda = 1550$ nm. The effective index is computed to be 1.8436. Figures 4 (d)–(f) show the first resonant mode's orthogonal components along the ρ , ϕ , and z directions, determined by solving Eq. (14).

Since the ring's radius is very large compared to the λ , the effective index of the first resonant mode is 1.8448, very close to the effective index of the waveguide.

With Eq. (38), the group index is determined to be 2.1292, corresponding to an expected FSR of 99.6 GHz based on Eq. (39). Figure 5 shows the transmission spectrum obtained with the numerical solution of Eq. (36). The spectral difference between the two dips, in other words, the FSR, is calculated to be 99.6 GHz, which agrees with the approximate number determined with Eq. (39).

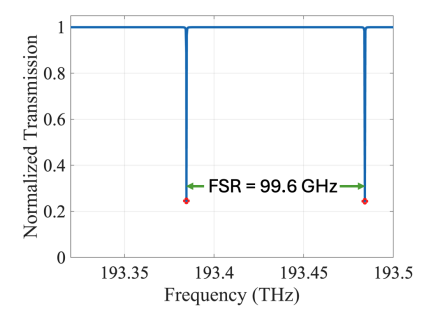


Fig. 5. Normalized transmission vs. excitation frequency obtained with the numerical solution of Eq. (36).

Figure 6 presents a detailed view of the resonance observed in both our numerical simulations and experimental measurements. To validate these simulations experimentally, we employed a setup with a primary pump laser operating with low power at 1550.183 nm to characterize the resonator's linewidth. Both results exhibit a Lorentzian shape with a linewidth (full width at half maximum) of 120 MHz. This narrow linewidth corresponds to a high quality factor (Qfactor = pump frequency/ $\Delta_{\rm FWHM}$) of 1.6 million, indicating a highly confined resonance. It is important to note that this Qfactor represents the total or loaded quality factor, defined as $1/Q = 1/Q_c + 1/Q_i$, and is distinct from the coupling quality factor (Q_c) and the intrinsic resonance quality (Q_i) of the ring. The average coupling quality factor, which characterizes the energy transfer efficiency between the waveguide and the ring, was numerically determined to be 2.2 million.

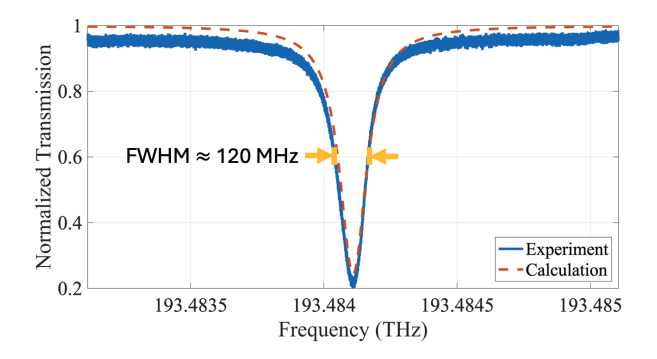


Fig. 6. Comparison of experimental (blue) and calculated (red) transmission spectra near the resonance.

The close correspondence between the numerical and experimental results validates the accuracy of our numerical model

and confirms the high performance of the device fabricated by Ligentec. The slight discrepancies between the simulated and measured spectra may be attributed to factors such as fabrication imperfections, thermal fluctuations, or minor deviations in the experimental setup, which are not fully accounted for in the model. Nonetheless, the overall agreement underscores the accuracy of our numerical model.

Figure 7 presents a comparative analysis of the calculated (top panel) and experimentally-measured (bottom panel) power spectra, showcasing the generation of an optical frequency comb using a bus waveguide coupled to a ring resonator. To validate these simulations experimentally, we employed a setup with a primary pump laser operating at 1550.183 nm and 230 mW, and an auxiliary laser at 1543.84 nm and 225 mW. For the LLE solution, we assume $\delta_0 = 4.4$, F = 2.6, $D_2 = -0.05$, and $\gamma = 0.9$. Both the simulation and experimental data confirm the formation of a frequency comb with an FSR of 99.6 GHz, demonstrating excellent agreement in this fundamental characteristic.

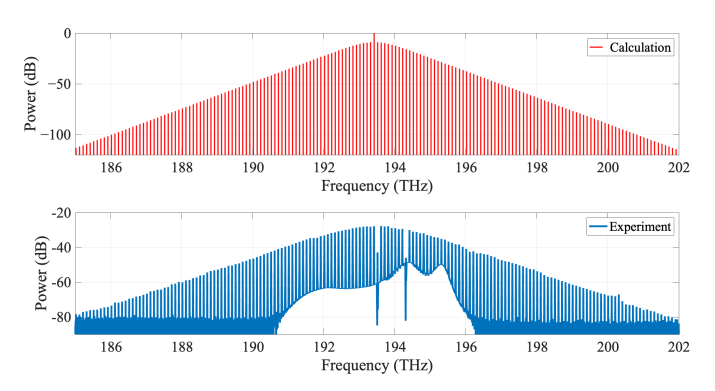


Fig. 7. Spectral power density comparison between calculated (top) and experimental (bottom) results.

The calculated spectrum (top panel) displays a highly regular and idealized comb structure characterized by sharp spectral lines with a hyperbolic-secant shape spanning a wide bandwidth. This spectrum represents the intrinsic behavior of the system as predicted by the Lugiato-Lefever equation, assuming ideal conditions. In contrast, the experimentally obtained spectrum (bottom panel) exhibits deviations from this ideal scenario. Notably, the noise floor is significantly higher in the experimental data, indicating the presence of noise sources not accounted for in the simulations. While the higher noise floor might suggest detector limitations, it is primarily attributed to the low power levels reaching the detectors due to losses from couplers and insertion losses in the experimental setup. This contrasts with the simulation, where the entire signal output is plotted.

Furthermore, the experimental spectrum displays additional spectral features, such as dips and broadened peaks, which are absent in the calculated results. These deviations may arise from various factors, including fabrication imperfections [3], thermal fluctuations [1], photodetector noise [21], [22], and non-ideal coupling conditions [23]. For instance, variations in the waveguide dimensions or surface roughness can lead to scattering losses and resonance shifts, affecting the comb's

spectral profile [3]. Similarly, temperature fluctuations can induce changes in the refractive index, altering the cavity's resonance frequencies [1]. It is important to note that both the primary pump and auxiliary laser peaks are filtered out in the experimental spectrum using fiber Bragg grating filters (FBG). The observed spectral features, along with the power-related noise floor, provide valuable insights into the non-ideal behavior of the fabricated device and highlight the challenges associated with achieving perfect agreement between simulations and experiments.

Despite these discrepancies, the overall agreement between the calculated and experimental spectra, particularly the consistent FSR, validates the accuracy of our numerical model and confirms the successful generation of an optical frequency comb with the designed device. The deviations observed in the experimental data underscore the importance of considering real-world factors, such as detector noise and fabrication imperfections when designing and characterizing integrated photonic devices.

VI. CONCLUSION

In this study, we presented a comprehensive numerical and experimental investigation of optical frequency comb generation in a silicon nitride microresonator coupled to a dielectric waveguide. We developed a robust numerical framework, combining compact mode solvers, coupled-mode theory, and the Lugiato-Lefever equation to accurately model the linear and nonlinear dynamics of the system. Our numerical simulations indicate the formation of a frequency comb with a free spectral range of 99.6 GHz, a result that was corroborated by our experimental measurements. The high quality factor of 1.6 million, determined from both simulation and experiment, demonstrates the low-loss characteristics of the fabricated device. The close agreement between our numerical predictions and experimental data validates the accuracy of our modeling approach. Discrepancies observed in the experimental spectrum, such as an elevated noise floor and additional spectral features, were attributed to limitations inherent in the experimental setup, including photodetector noise and fabrication imperfections. Future work will focus on mitigating the experimental limitations and further optimizing the device performance to achieve even closer agreement between simulations and experiments, contributing to the realization of integrated, chip-scale frequency comb sources with unprecedented stability and efficiency.

ACKNOWLEDGMENT

This work has been supported in part by cooperative agreements with the National Center for Manufacturing Sciences 2022138-142232 and 2023200-142386, which are subcontracts from the US-DoD cooperative agreements HQ0034-20-2-0007 and HQ0034-24-2-0001 respectively. The authors acknowledge useful discussions with J. P. Cahill, T. Mahmood, and W. Zhou of the Army Research Laboratory and G. Moille and K. Srinivasan of NIST and UMD-JQI.

REFERENCES

- T. J. Kippenberg, R. Holzwarth, and S. A. Diddams, "Microresonatorbased optical frequency combs," *Science*, vol. 332, no. 6029, pp. 555– 559, 2011.
- [2] G. Moille, Q. Li, T. C. Briles, S.-P. Yu, T. Drake, X. Lu, A. Rao, D. Westly, S. B. Papp, and K. Srinivasan, "Broadband resonator-waveguide coupling for efficient extraction of octave-spanning microcombs," *Optics Letters*, vol. 44, no. 19, pp. 4737–4740, 2019.
- [3] G. Moille, D. Westly, N. G. Orji, and K. Srinivasan, "Tailoring broadband kerr soliton microcombs via post-fabrication tuning of the geometric dispersion," *Applied Physics Letters*, vol. 119, no. 12, 2021.
- [4] A. D. Ludlow, M. M. Boyd, J. Ye, E. Peik, and P. O. Schmidt, "Optical atomic clocks," *Reviews of Modern Physics*, vol. 87, no. 2, pp. 637–701, 2015.
- [5] N. Picqué and T. W. Hänsch, "Frequency comb spectroscopy," *Nature Photonics*, vol. 13, no. 3, pp. 146–157, 2019.
- [6] H. Hu and L. K. Oxenløwe, "Chip-based optical frequency combs for high-capacity optical communications," *Nanophotonics*, vol. 10, no. 5, pp. 1367–1385, 2021.
- [7] A. Pasquazi et al., "Micro-combs: A novel generation of optical sources," *Physics Reports*, vol. 729, pp. 1–81, 2018.
- [8] M. Soroush et al., "Predicting broadband resonator-waveguide coupling for microresonator frequency combs through fully connected and recurrent neural networks and attention mechanism," ACS Photonics, vol. 10, no. 6, pp. 1795–1805, 06 2023.
- [9] A. Yariv, "Coupled-mode theory for guided-wave optics," *IEEE Journal of Quantum Electronics*, vol. 9, no. 9, pp. 919–933, 1973.
- [10] M. Chin and S. Ho, "Design and modeling of waveguide-coupled single-mode microring resonators," *Journal of Lightwave Technology*, vol. 16, no. 8, pp. 1433–1446, 1998.
- [11] E. S. Hosseini, S. Yegnanarayanan, A. H. Atabaki, M. Soltani, and A. Adibi, "Systematic design and fabrication of high-q single-mode pulley-coupled planar silicon nitride microdisk resonators at visible wavelengths," *Optics Express*, vol. 18, no. 3, pp. 2127–2136, 2010.
- [12] L. A. Lugiato and R. Lefever, "Spatial dissipative structures in passive optical systems," *Physical Review Letters*, vol. 58, no. 21, p. 2209, 1987.
- [13] Y. K. Chembo and N. Yu, "Modal expansion approach to optical-frequency-comb generation with monolithic whispering-gallery-mode resonators," *Phys. Rev. A*, vol. 82, p. 033801, Sep 2010.
- [14] Y. K. Chembo and C. R. Menyuk, "Spatiotemporal model for kerr comb generation in whispering gallery mode resonators," *Phys. Rev. A*, vol. 87, p. 053852, 2013.
- [15] F. Castelli, M. Brambilla, A. Gatti, F. Prati, and L. A. Lugiato, "The LLE, pattern formation and a novel coherent source," *The European Physical Journal D*, vol. 71, no. 4, p. 84, 2017.
- [16] D. C. Cole, A. Gatti, S. B. Papp, F. Prati, and L. Lugiato, "Theory of kerr frequency combs in fabry-perot resonators," *Phys. Rev. A*, vol. 98, p. 013831, Jul 2018.
- [17] E. Simsek, "Practical vectorial mode solver for dielectric waveguides based on finite differences," Opt. Lett., vol. 50, no. 12, pp. 4102–4105, Jun 2025. [Online]. Available: https://opg.optica.org/ol/abstract.cfm? URI=ol-50-12-4102
- [18] E. Simsek, A. Niang, R. Islam, L. Courtright, P. Shandilya, G. M. Carter, and C. R. Menyuk, "A mixed-field formulation for modeling dielectric ring resonators and its application in optical frequency comb generation," *Scientific Reports*, vol. 15, no. 1, p. 35098, 2025.
- [19] L. B. Felsen and S. Shin, "Rays, beams, and modes pertaining to the excitation of dielectric waveguides," *IEEE Transactions on Microwave Theory and Techniques*, vol. 23, no. 1, pp. 150–161, 1975.
- [20] R. J. LeVeque, Finite Difference Methods for Differential Equations: Class notes for AMath 585–6. University of Washington, 2005, pp. 21–23.
- [21] E. Simsek, I. M. Anjum, T. F. Carruthers, C. R. Menyuk, J. C. Campbell, D. A. Tulchinsky, and K. J. Williams, "Fast evaluation of RF power spectrum of photodetectors with windowing functions," *IEEE Transactions on Electron Devices*, vol. 70, no. 7, pp. 3643–3648, 2023.
- [22] I. M. Anjum, E. Simsek, S. E. J. Mahabadi, T. F. Carruthers, C. R. Menyuk, J. C. Campbell, D. A. Tulchinsky, and K. J. Williams, "Use of evolutionary optimization algorithms for the design and analysis of low bias, low phase noise photodetectors," *Journal of Lightwave Technology*, vol. 41, no. 23, pp. 7285–7291, 2023.
- [23] S. Cheung, Y. Yuan, Y. Peng, G. Kurczveil, S. Srinivasan, Y. Hu, A. Descos, D. Liang, and R. G. Beausoleil, "Demonstration of a 17× 25 gb/s heterogeneous III-V/Si DWDM transmitter based on (de-interleaved quantum dot optical frequency combs," *Journal of Lightwave Technology*, vol. 40, no. 19, pp. 6435–6443, 2022.